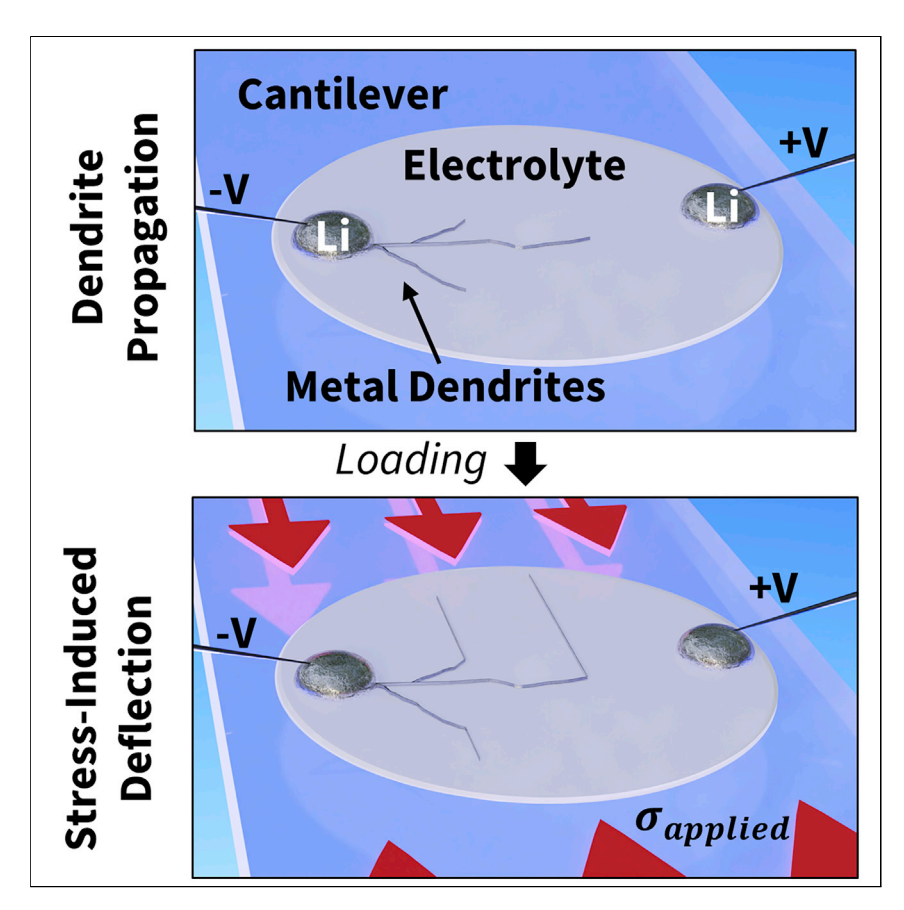
Joule



Article

Controlling dendrite propagation in solidstate batteries with engineered stress



Metal dendrites penetrate and short-circuit solid electrolytes at commercially relevant current densities. Whether dendrites grow by internal chemical reduction of lithium or because of mechanical stresses has been a topic of debate. Herein, operando microscopy demonstrates that dendrites kink dramatically at the onset of mechanical loading and can be deflected enough to avert short circuits. The observed behavior is indicative of fracture-governed dendrite propagation. From this newfound mechanistic understanding, we propose means to engineer residual stresses in solid-state batteries, thereby preventing short-circuit failures.

Cole D. Fincher, Christos E. Athanasiou, Colin Gilgenbach, Michael Wang, Brian W. Sheldon, W. Craig Carter, Yet-Ming Chiang

ychiang@mit.edu

Highlights

Growing dendrites deflect in response to applied loading, averting short circuits

Dendrites propagate due to plating-induced fracture of the electrolyte

Stresses on the order of 150 MPa deflect and arrest dendrites in oxide electrolytes

Engineered residual thermal stresses can deflect dendrites in conventional cells

Fincher et al., Joule 6, 1–16
December 21, 2022 © 2022 Elsevier Inc.
https://doi.org/10.1016/j.joule.2022.10.011

Joule



Article

Controlling dendrite propagation in solid-state batteries with engineered stress

Cole D. Fincher,¹ Christos E. Athanasiou,^{2,3} Colin Gilgenbach,¹ Michael Wang,¹ Brian W. Sheldon,² W. Craig Carter,¹ and Yet-Ming Chiang^{1,4,*}

SUMMARY

Metal-dendrite penetration is a mode of electrolyte failure that threatens the viability of metal-anode-based solid-state batteries. Whether dendrites are driven by mechanical failure or electrochemical degradation of solid electrolytes remains an open question. If internal mechanical forces drive failure, superimposing a compressive load that counters internal stress may mitigate dendrite penetration. Here, we investigate this hypothesis by dynamically applying mechanical loads to growing dendrites in Li_{6.6}La₃Zr_{1.6}Ta_{0.4}O₁₂ solid electrolytes. Operando microscopy reveals marked deflection in the dendrite growth trajectory at the onset of compressive loading. For sufficient loading, this deflection averts cell failure. Using fracture mechanics, we quantify the impact of stack pressure and in-plane stresses on dendrite trajectory, chart the residual stresses required to prevent short-circuit failure, and propose design approaches to achieve such stresses. For the materials studied here, we show that dendrite propagation is dictated by electrolyte fracture, with electronic leakage playing a negligible role.

INTRODUCTION

Pairing Li metal with non-flammable solid electrolytes promises to enable safer and higher energy density batteries than Li-ion cells using flammable liquid electrolytes. 1 However, at practical current densities, metal filaments (generally referred to as dendrites) are known to pierce solid electrolytes and short-circuit cells. 1,2 Despite extensive study beginning nearly 50 years ago,³⁻⁹ there is disagreement as to the mechanism(s) by which dendrites penetrate inorganic electrolytes. Most recent studies argue that failure occurs via one of two mechanisms. The first interpretation, based on the low fracture toughness of inorganic solid electrolytes and the crack-like morphology of many metal dendrites, 8,10-12 holds that metal-dendrite penetration is driven by mechanical fracture: that metal insertion into flaws in the electrolyte at the metal—solid electrolyte interface leads to stress buildup exceeding the fracture strength of the solid electrolyte. 4,8,9,11,13 The second conjecture, based upon observations of Li-metal nucleation within the bulk of the electrolyte, posits that failure is driven by electrical and electrochemical degradation: that electronic conduction enables internal reduction of lithium ions causing solid-phase Li metal to form within the solid electrolyte. 3,5,6,14 To design future electrolytes that are resistant to dendrites, the fundamental drivers underlying dendrite growth must be understood.

We develop an experimental methodology and fracture mechanics model that elucidates the interaction between the electrochemical and mechanical forces underlying metal-dendrite propagation. We observe the propagation of lithium metal dendrites

CONTEXT & SCALE

Pairing Li metal with nonflammable solid electrolytes promises to enable safer, highercapacity Li-ion batteries. However, at practical current densities, metal filaments (termed "dendrites") form on the metal electrode during charging, eventually penetrating the electrolyte and shorting the cell. Whether this growth is due to mechanical failure or chemical degradation has remained a topic of debate. In this work, we provide direct observations that show not only that dendrites are driven by mechanical failure of the electrolyte but also that mechanical stresses can be used to control dendrite trajectory and avert cell failure. While most previous electrolyte engineering efforts focus on increasing the current density at which dendrites initiate, our findings suggest a new paradigm: that electrolytes can be engineered to inhibit dendrite propagation. Based upon this principle, we outline design approaches suitable for deflecting metal dendrites in solid-state batteries.





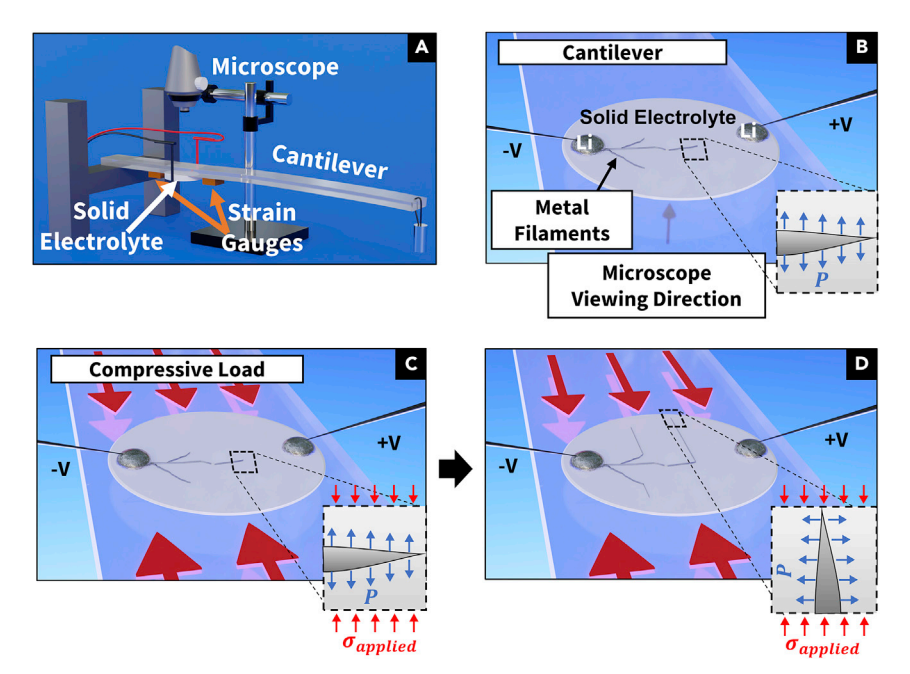


Figure 1. Observing the response of metal dendrites to applied loads

(A) A microscope observes a solid-state cell consisting of lithium metal electrodes adhered to a thin solid electrolyte disk (1/2" diameter), fixed rigidly to a transparent cantilever. Weight applied to the end of the cantilever induces strain in the bar and the electrolyte. This strain is measured in real time using strain gauges.

- (B) The plan-view cell geometry and dendrite orientation in the load-free configuration. Applied current produces plating-induced pressure (P) inside metal-filled flaws at the anode/electrolyte interface. This pressure acts normally to the flaw surface, wedging open the flaw and allowing metal dendrites to propagate through the cell.
- (C) The cell under load. Weight placed on the end of the cantilever (see A) generates compressive strains in the cantilever and the electrolyte. Resulting compressive stress ($\sigma_{applied}$) acts along the cantilever's axis and opposes the plating-induced pressure P causing crack opening and dendrite propagation.
- (D) Dendrite deflection when propagating under compressive load. For $\sigma_{applied}=200$ MPa, the metal propagation direction turned about 90° to align with the loading axis.

through a model solid electrolyte, Li $_{6.6}$ La $_{3}$ Zr $_{1.6}$ Ta $_{0.4}$ O $_{12}$ (LLZTO), under sequential and simultaneous electrochemical and mechanical stimulation. Using fracture mechanics, we predict the mechanical stress state required to arrest or deflect dendrites and compare those results with experiments. Finally, we propose a design strategy that would deflect or arrest dendrites by introducing residual compressive stresses into the electrolyte during the fabrication of solid-state batteries.

RESULTS AND DISCUSSION

Response of metal dendrites to electrical and mechanical stimulation

If plating-induced pressure (P in Figure 1B) drives dendrite growth, superimposing a compressive stress ($\sigma_{applied}$ in Figure 1C) should balance internal stress buildup and mitigate penetration. We investigate this hypothesis by applying stresses mechanically, but such stresses could also be produced with residual thermal or chemically induced stresses. Using a geometry in which two lithium metal electrodes are adhered to the surface of a thin disk of LLZTO electrolyte, we plate lithium dendrites through the plane of the electrolyte. This solid-state cell (\sim 1.27-cm diameter) is mounted on a cantilever beam (Figures 1A and 1B), oriented such that bending the beam results in an applied stress $\sigma_{applied}$ orthogonal to the electric field direction (Figure 1C). By using a transparent material for the cantilever beam, operando optical microscopy can be conducted while varying current and mechanical load

¹Department of Materials Science and Engineering, Massachusetts Institute of Technology, Cambridge, MA, USA

²School of Engineering, Brown University, Providence, RI, USA

³Center for Bits and Atoms, Massachusetts Institute of Technology, Cambridge, MA, USA

⁴Lead contact

^{*}Correspondence: ychiang@mit.edu https://doi.org/10.1016/j.joule.2022.10.011





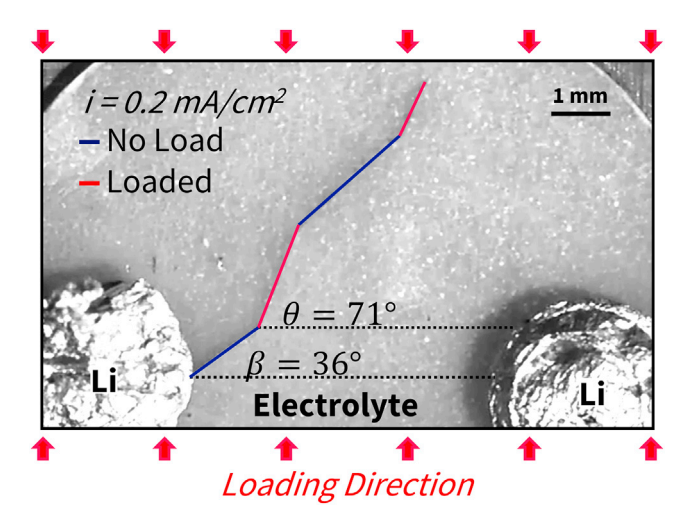


Figure 2. The response of a metal dendrite to electrochemical and mechanical loadings
Deflection of a propagating dendrite in response to load. Initially, the dendrite propagates along
the segment highlighted in blue under galvanostatic conditions (0.2 mA/cm²). Upon application of
70 MPa compressive stress, deflection of the dendrite along the first red segment occurred. Load
removal, and reloading, produced the second blue and red segments, respectively. Image
recorded while viewing through the cantilever (viewing direction opposite to that in Figure 1B);
solid electrolyte is 90 μm thick. All plating occurred at voltages within the LLZTO electrolyte window
(voltage and current data available in the supplemental information).

independently. Thus, in this work, we study the impact of applied stresses upon propagating dendrites large enough to be observed by optical microscopy ($\geq 20~\mu m$). All Li-metal dendrites observed here appeared to originate from the Li/LLZTO interface; in no instance did we observe nucleation and growth within the LLZTO itself leading to a dendrite. While applied stress may also affect dendrite initiation, those effects are not specifically studied here.

We observed that metal dendrites exhibit a correlated response to applied mechanical loads (Figures 2, 3, and 4). Results for a 90 μm thick LLZTO electrolyte disk are shown in Figure 2. A dendrite propagating under 0.2 mA/cm² current density (current divided by the initial Li-metal electrode area) was subjected to 70 MPa applied compression and then unloaded. The path of the dendrite under no applied load is highlighted in blue, while the segment propagated under load is highlighted in red. Micrographs with no highlighting are shown in the supplemental information. Upon loading, a clear deflection of the dendrite toward the loading axis is observed. Upon removal of the load, the dendrite turned back toward its original propagation direction. The tendency for dendrites to align with the applied load is consistent with the propagation of a pressurized crack. Continuous metal plating results in a pressure buildup within the metal protrusion. This results in a pressure on the flaw surface (P in Figure 1B), which drives propagation. Compressive forces (i.e., $\sigma_{applied}$ in Figure 1C) can act to close cracks and inhibit propagation perpendicular to the axis of compression. Therefore, under increased load, cracks should turn toward the axis of compression, consistent with the experimental finding in Figure 2.

At higher applied loads, dendrites deflect into close alignment with the loading axis (Figure 3). A 30 μ m thick electrolyte disk was successively loaded and unloaded as metal dendrites propagated under 0.3 mA/cm² galvanostatic current density (Figures 3A and 3B). In this experiment, 200 MPa compressive loads produced dendrite growth nearly aligned with the loading direction, even for current densities





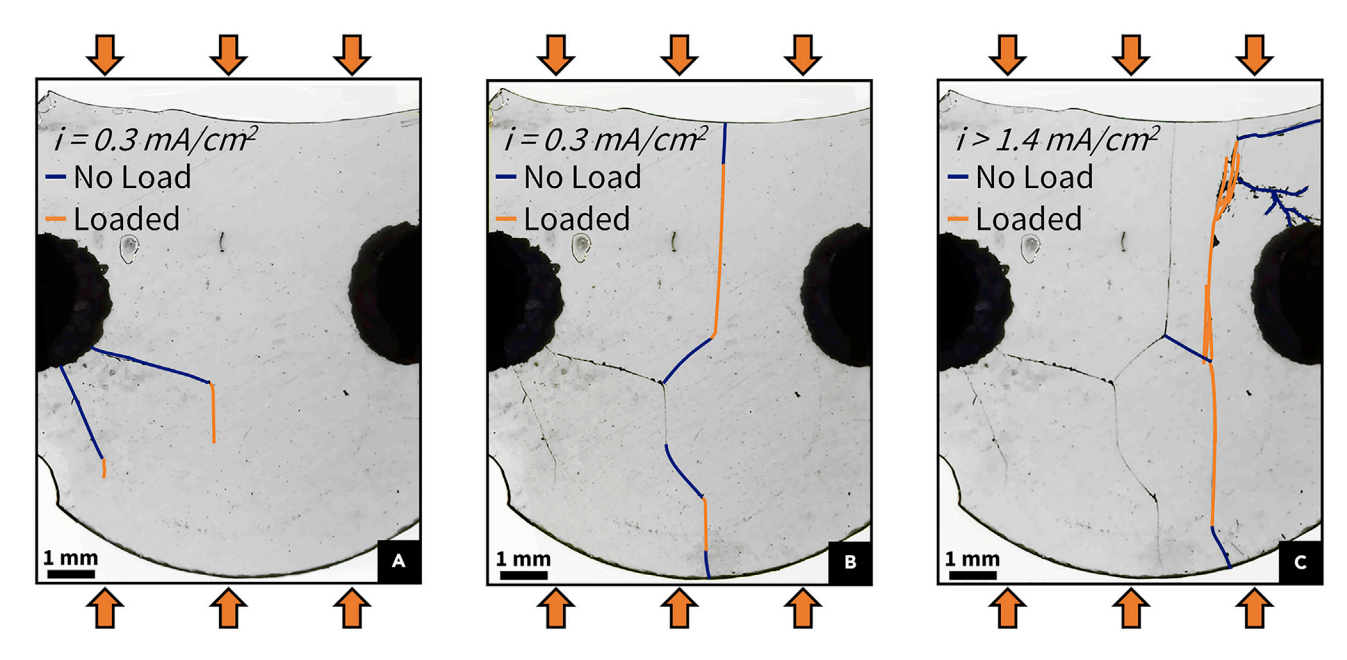


Figure 3. The response of propagating metal dendrites to applied loads in a 30 µm thick electrolyte, imaged via operando microscopy

Metal dendrites initiated at 1.1 mA/cm² galvanostatic current density using the cell configuration from Figure 1. Dendrite segments are highlighted in each frame. The sequence (A)–(C) is chronological. All plating occurred at voltages within the LLZTO electrolyte stability window (voltage and current

data available in the supplemental information).

(A and B) Metal dendrites propagating under 0.3 mA/cm² galvanostatic current density: the compressive stress in (A) and (B) resulted in dendrite growth nearly aligned with the loading direction. When plating occurred without applied loads, dendrites propagated toward the counter-electrode. For the

growth shown in (B), the dendrites propagated toward the electrolyte edges, where the dendrites appeared to arrest. (C) Dendrite growth spurred by increasingly high current densities: once the load was re-applied, dendrites grew toward loading direction, even at increasing current densities up to 5.6 mA/cm². After the load was removed, metallic dendrites grew toward the stripping electrode and subsequently electrically shorted the cell.

up to 5 mA/cm² (Figure 3C). Kinking events associated with the formation of the complex network of cracks in the upper right-hand corner of Figure 3C may be attributed to microstructural heterogeneities (e.g., grain level anisotropy in elastic properties). After load removal, the dendrites grow toward the stripping electrode and electrically short the cell (seen in Figure 3C). This observation demonstrates that compressive stresses can prevent electrical shorting.

Results for thick electrolyte samples were similar. In Figure 4, metal filaments in a thicker solid electrolyte disk (250 μ m, as compared with 30 μ m shown in Figure 3) are also observed to deflect under load. Growing dendrites deflected toward the loading axis (Figures 4C–4E), with the crack-plane oriented normal to the page (Figure 4F). This result shows that compressive stresses may be used to mitigate dendrite propagation in electrolyte samples of similar thickness to those commonly studied in literature.

While the experiments in Figures 2, 3, and 4 demonstrate the effect of stress applied perpendicular to the plating direction, Figure 5 displays the impact of a stress applied parallel to the plating direction. After load onset, the dendrites kink toward the stripping electrode, into the direction of compression. Thus, while the loading configuration shown in Figures 1, 2, 3, and 4 mitigates dendrite-induced shorting, the load in Figure 5 facilitates such shorting.

All experiments here showed that compressive stresses impact both the propagation direction and the orientation of metal dendrites in solid electrolytes. The deflection increases with the load's magnitude: a 70 MPa load produced a small deviation





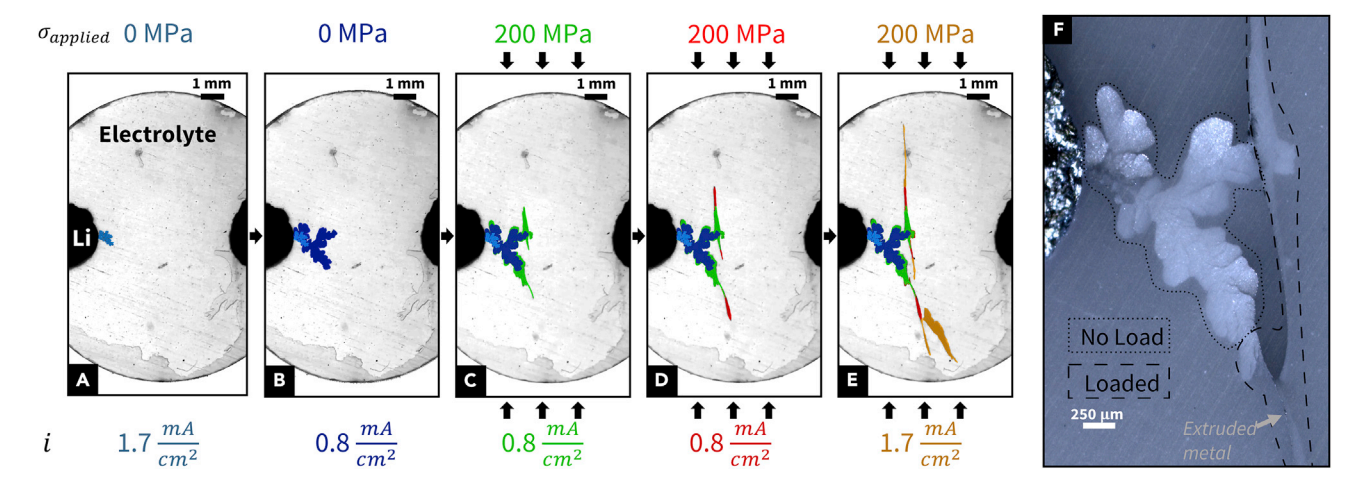


Figure 4. The response of propagating metal dendrites to applied loads in a 250 µm thick electrolyte

(A–E) Metal dendrites initiated at 1.7 mA/cm² galvanostatic current density using the cell geometry shown in Figure 1. Figures 4A–4E demonstrate the progressive growth, deflection, and arrest of dendrites as the load and current density across the cell are varied. Growth-segments from each subfigure are highlighted in a separate color. All images for (A)–(E) were recorded using strong backlighting (i.e., light positioned below the transparent cantilever).

(F) A micrograph recorded after the end of the test, with the illuminating light source positioned above the cantilever. The dotted line outlines metal growth plated without applied compression. After the load was applied, the crack-plane rotated into alignment with the out-of-the-page direction, producing the metal enclosed by the dashed line in (F). All plating occurred at voltages within the LLZTO electrolyte stability window (voltage and current data available in the supplemental information).

in the dendrite propagation direction. Larger applied loads ($\sigma_{applied} \geq 200$ MPa) produced dendrite growth nearly parallel to the loading axis. Stated plainly, compressive loads can deflect metal dendrites to the extent that electrical short-circuiting of the solid electrolyte is completely averted. During preparation of this manuscript, we became aware of a recent pre-print from McConohy et al., ¹⁵ in which a correlation is observed between the strain applied to a solid electrolyte and the initial dendrite growth morphology (at a few micrometer length scale). Those results are qualitatively consistent with the present findings; as we show, regardless of the initial orientation of a growing dendrite, the direction of propagation can be changed by an imposed stress field.

Fracture mechanics model for dendrite deflection

From fracture mechanics, we develop a model to describe the dendrite trajectory under mechanical loading. We will use this model to interpret our experimental results and later to provide criteria for deflecting dendrites (thus averting electrical shorting). Dendrites are modeled as slit-like metal-filled flaws initially oriented at angle β from the horizontal (Figure 6A) in a homogeneous and isotropic solid electrolyte. The planar electrolyte/electrode interface is held with fixed horizontal displacement. We then assume that metal plating into the flaw leads to a uniform pressure of P normal to the flaw face. In the absence of any other stresses in the electrolyte, this plating-induced pressure P causes the dendrite to propagate forward without kinking. When an additional load is applied to the solid electrolyte in the vertical direction (σ_{vv}), the energetically preferred path for dendrite propagation is at a kinked angle from its initial orientation, 16,17 as seen in Figure 6A. The stress state in front of the crack tip is then a result of the superposition of the plating-induced pressure and the applied load. The most favorable propagation angle (θ in Figure 6A) maximizes the local mode I stress intensity factor for an infinitesimal extension of the crack tip. The derivation underlying this model is detailed in analytical methods.



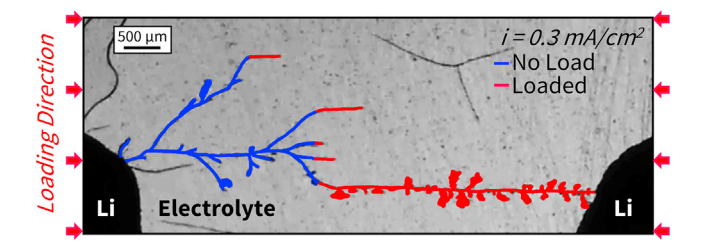


Figure 5. The response of a metal dendrite to mechanical loading along the horizontal direction Deflection of propagating dendrites in response to an applied load (oriented here in the horizontal direction). Initially, the dendrites propagate along the segments highlighted in blue under galvanostatic conditions (0.3 mA/cm²). Upon application of 500 MPa compressive stress, dendrites deflect toward the loading direction (shown in red). The solid electrolyte is 90 μm thick. Voltage and current data available in the supplemental information. Uncolored black lines within the electrolyte represent precracks due to handling and processing.

This model provides a means to assess whether the experimental observations are consistent with fracture-governed dendrite propagation. If filament propagation is driven purely by mechanical fracture, the plating-induced pressure P that would be inferred from experiments (based upon observed deflection angle for a dendrite under a given applied load) would match the fracture stress expected from an ex situ test (called $\sigma_{critical}$). If, on the other hand, propagation is governed largely by chemical degradation, as would be the case for failure via electronic leakage, then the inferred P should be much lower than $\sigma_{critical}$. We first estimate $\sigma_{critical}$ by drawing on the analysis of Beuth et al., 18 who studied propagation of through-thickness cracks in a thin plate of the geometry in Figure 2. Applying their analysis to the 90 μm-thick LLZTO disk studied here (detailed further in analytical methods) yields $\sigma_{critical}$ values between 65 and 120 MPa (for LLZTO fracture toughness, K_{IC} , of 1–2 MPa \sqrt{m}). ^{2,19} The plating-induced pressure P is then independently inferred from the change in filament propagation angle under a known load. From Figure 2, the measured angles of $\beta = 36^{\circ}$ and $\theta = 71^{\circ}$ under an applied load of 70 MPa yield P = 115 MPa, which is indeed similar in magnitude to $\sigma_{critical}$. The corresponding stress intensity factor, K = 1.8 MPa \sqrt{m} , also matches closely with the expected K_{IC} for LLZO.¹⁸ This comparison supports the conclusion that dendrite propagation is a fracture process in which the plating-induced pressure P is approximately the critical stress required for fracture (i.e., the fracture stress).

The model results capture key aspects of experimental behavior and provide design criteria for averting failure. The results in Figure 6 show that in-plane stresses slightly larger than P should deflect dendrites of any initial orientation, β , to a final angle $\theta = 90^{\circ}$, thereby averting cell shorting. Figure 6B plots the most energetically favorable propagation angle as a function of the load (given as σ_{vv}/P) and the initial crack inclination, β . For a given β , compressive σ_{yy} increases the propagation angle θ for all β (consistent with Figure 6), whereas tensile σ_{vv} decreases β . A critical stress exists for reaching the design objective $\theta = 90^{\circ}$. For some range of $\theta < 90^{\circ}$, short-circuiting may still be avoided depending on the thickness and lateral dimensions of the solid electrolyte. However, for compressive stress, θ is always larger than β until β reaches 90°. Note that a relatively small overstress provides a substantial margin of safety; Figure 6C shows that a compressive stress only 10% larger than P (i.e., $\sigma_{vv} \approx$ 1.1P) forces $\theta = 90^{\circ}$ for all initial angles β . This result is consistent with the experimental observation (Figures 3 and 4) that a 200 MPa load repeatedly deflects all observed filaments to $\theta \approx 90^{\circ}$. In the following section, we model the critical stress and corresponding engineering requirements for dendrite deflection in solid-state battery architectures.





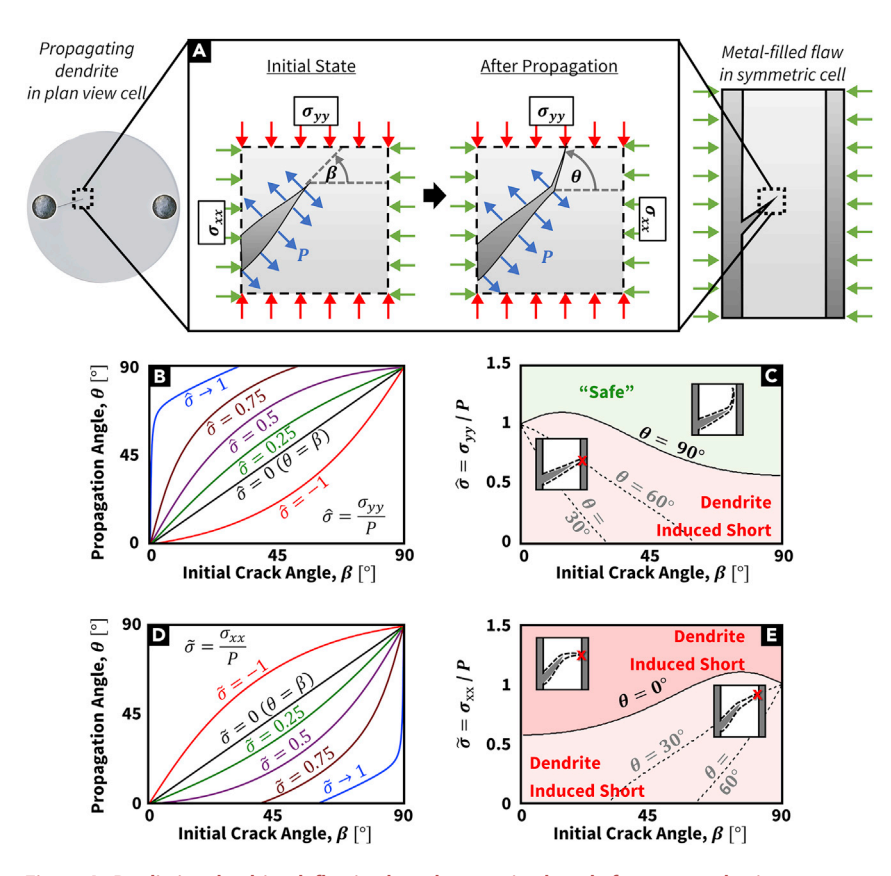


Figure 6. Predicting dendrite deflection based upon mixed-mode fracture mechanics

(A) Schematic of loading conditions used in modeling kinked propagation of metal dendrites. The most energetically favorable propagation angle θ as a function of the flaw inclination β is obtained. Both angles are measured counter-clockwise from the horizontal. Two loads are present for this flaw: a plating-induced stress P acting normal to the flaw surface, with an additional load (σ_{xx} and / or σ_{yy}) due to external forces or from residual stresses present in the solid electrolyte. This model applies to two (equivalent) loading scenarios: (1) The kinking of propagating metal dendrites upon the application of applied load, shown for a plan-view cell on the left side of the subfigure and (2) the kinking of a metal-filled flaw at the anode/electrolyte interface at the instant propagation begins (seen in the right side of the subfigure).

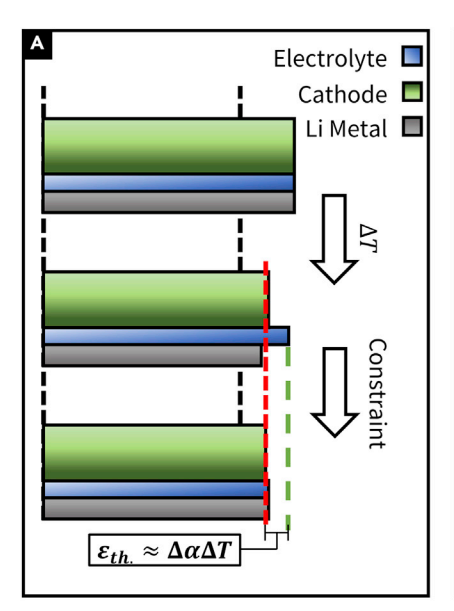
- (B) The most energetically favorable propagation angle as a function of initial crack-inclination angle β for different values of $\widehat{\sigma} = \sigma_{yy}/P$. The black curve represents the case where the only stress in the system is P, (i.e., $\widehat{\sigma}=0$), such that $\theta=\beta$. Increasingly positive $\widehat{\sigma}$ values represent increasing compressive loadings, which then increase the value of θ relative to that for $\widehat{\sigma}=0$, causing deflection. The series denoted $\widehat{\sigma}\to 1$ represents the solution for θ as $\widehat{\sigma}$ approaches 1. In the limit where $\theta=90^\circ$, the metal dendrite cannot reach the counter-electrode regardless of the lateral dimensions of the electrolyte. The results in this work indicate that P is approximately equal to the fracture stress of the electrolyte.
- (C) The value of $\hat{\sigma}$ required to produce $\theta=90^\circ$, $\theta=60^\circ$, and $\theta=30^\circ$ as a function of crack inclination β .
- (D) The most energetically favorable propagation angle θ as a function of inclination angle β for different values of $\tilde{\sigma} = \sigma_{xx}/P$. Increasingly positive $\tilde{\sigma}$ represent increasing compressive stack pressures, where stack pressures approaching the magnitude of P tend to decrease the propagation angle relative to $\tilde{\sigma} = 0$. The series denoted $\tilde{\sigma} \to 1$ represents the solution for θ as $\tilde{\sigma}$ approaches 1.
- (E) The value of $\tilde{\sigma}$ required to produce $\theta=0^{\circ}$, $\theta=30^{\circ}$, and $\theta=60^{\circ}$ as a function of crack inclination β .

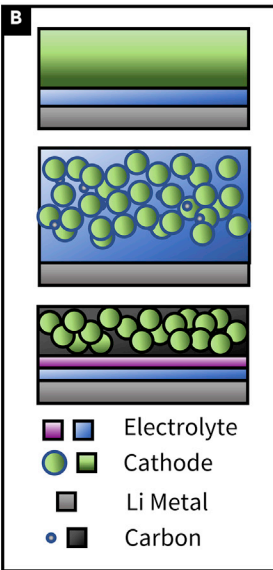
Engineering solid-state batteries for dendrite deflection

The insights described above are transferable to realistic solid-state battery architectures. The previous sections demonstrate two key points: (1) that dendritic









C Material	lpha [10 ⁻⁵ K ⁻¹]	lpha Ref. Number	<i>E'</i> [GPa]	<i>E'</i> Ref. Number
Li ₇ La ₃ Zr ₂ O ₁₂ (LLZO)	1.5	26	200	43
$\text{Li}_{1+x}\text{Al}_x\text{Ti}_{2-x}(\text{PO}_4)_3$ (LATP)	1.1	30	160	29,46
Li ₁₀ GeP ₂ S ₁₂ (LGPS)	3.5	27	30	28, 47
Li _x PO _y N _z (LiPON)	1	48	93	49
LiFePO ₄ (LFP)	4.5	25	165	25
LiNi _{0.33} Mn _{0.33} Co _{0.33} O ₂ (NMC)	1.3	50,51	260	50

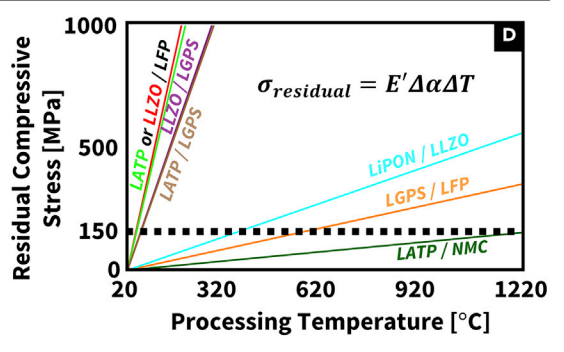


Figure 7. Thermally induced stresses in laminate cell architectures

(A) Schematic showing how residual stresses arise in laminate structures from differential thermal contraction.

(B) Candidate geometries in which residual stresses can be introduced by differential thermal contraction. In the upper left, a layered cathode adhered to an electrolyte-sheet and Li-anode. In the upper right, a multi-layered solid electrolyte paired with a composite-cathode and Li-metal anode. In the lower right, an example of co-sintered composite electrolyte/cathode employed against a Li-metal anode.

(C) The biaxial modulus and the coefficient of thermal expansion for representative cathodes and electrolytes. Each of these materials are representative of a broader class of solid electrolytes or electrodes: LLZTO is representative of oxide electrolytes, 24,25 Li₁₀GeP₂S₁₂ (LGPS) is representative of crystalline sulfide electrolytes, 26,27,28,29 Li_{1+x}Al_xTi_{2-x}(PO₄)₃ (LATP) is representative of LISICON electrolytes, 30,31,32 and nickel manganese cobalt oxide 33,34,35 (NMC) or lithium Iron phosphate (LFP)³⁶ are representative of various classes of cathodes. 33,34

(D) The residual compressive stress at the solid-electrolyte/cathode interface. According to Figure 5, compressive stresses on the order of P and larger should deflect metal dendrites, mitigating short-circuiting. For representative material properties and flaw size, $P \approx 150$ MPa. Individual series represent separate sets of electrolyte/cathode or electrolyte/electrolyte assemblies. For any given label, the first of two constituents listed (i.e., A in A/B) represents the anode-facing material. The compressive stress plotted represents the biaxial stress in the electrolyte plane, acting normally to the stack direction.

propagation is a largely stress-driven event and (2) that in-plane stresses larger than the fracture stress can be used to deflect dendrites, to an extent that prevents electrical short circuits. Such dendrite deflection can delay cell failure and avert uncontrolled discharge commonly associated with electrical shorting. For any electrolyte system with known fracture stress, the model in Figure 6 outlines the critical stress required to safely deflect dendrites. Beyond externally applied stresses, the required in-plane stresses necessary to deflect dendrites can be produced by other means. In fact, Qi et al. discuss ion-exchange processes, laser shot peening, or ion-implantation as possible methods for introducing residual compressive stresses into solid electrolytes. ^{13,20}

Here, we show that desired in-plane residual stresses can be engineered through thermal expansion mismatch between cell components in a prototypical solid-state lithium battery. Consider a solid-electrolyte layer bounded by a lithium metal negative electrode and an oxide cathode (upper portion of Figure 7A). Upon cooling of the structure, a mismatch in the thermal expansion coefficients of the constituent materials lead to mismatched thermal expansion between cell parts. Assuming no delamination between the Li-solid electrolyte and solid electrolyte cathode interfaces, thermal expansion mismatch between layers will result in a residual stress (seen in the bottom portion of Figure 7A). However, the very low yield stress of Li metal (~1 MPa^{21–23}) indicates that it will flow to relieve the resulting stress. On the





other hand, a relatively rigid solid electrolyte and cathode will support thermal expansion mismatch stresses. To achieve high energy density and fast charging, it is furthermore desirable that the electrolyte be thin relative to the cathode. In this case, the residual stress will be primarily borne by the solid electrolyte, as desired. If the cathode has a higher coefficient of thermal expansion than the electrolyte, the electrolyte will experience a residual compressive stress after cooling from the stress-free state at elevated temperature. An alternate approach to producing the requisite compressive biaxial stress in a solid-electrolyte layer is to laminate two solid electrolytes with different thermal expansion coefficients (Figure 7B), in which case the electrolyte of lower α receives the compressive stress. In both cases, the residual compressive stress is expressed as

$$\sigma = E' \varepsilon_{th} = E' \Delta \alpha \Delta T$$

where σ is the in-plane stress (σ_{yy} from the right side of Figure 6A) at the cathode-electrolyte interface, E' is the electrolyte biaxial elastic modulus, ε_{th} is the strain induced by the cathode/electrolyte thermal expansion mismatch, $\Delta\alpha$ is the difference in thermal expansion coefficients of the anode-facing material and its counterpart. If there is no mechanical relaxation (i.e., bending, creep, or interfacial delamination), then the resulting residual compression will act to deflect dendrites as in Figure 6. From the analysis in the previous section, P can be taken as $\sigma_{crit.}$ ($\approx \frac{K_{IC}}{1.12\sqrt{\pi a}}$ for this loading condition, with representative K_{IC} and a as 1 MPa \sqrt{m} and 10 μ m). We note that good adhesion between adjacent layers is necessary to preserve residual stress. Residual compressive stresses above 1 GPa are commonly observed in many thin films and coatings, 36 providing evidence of good bonding. Therefore, lower stress levels of \sim 150 MPa as desired here should be readily achievable. Nonetheless, for any given pair of materials, we anticipate that adhesion will have to be characterized and investigated with system-specific experiments.

Figure 7C lists biaxial moduli and thermal expansion coefficient values for several Li-ion cathodes and electrolytes. Notice that LiFePO₄ (LFP)²⁴ has a higher α than the three widely studied solid electrolytes listed (LLZTO, 26 Li₁₀GeP₂S₁₂ $(LGPS)^{27,30}$ and $Li_{1+x}Al_xTi_{2-x}(PO_4)_3$ $(LATP)^{31,37}$). Plotted in Figure 7D are lines of thermal residual stress versus processing temperature (assuming a quench to $T_1 = 20$ °C) for several solid electrolyte-cathode and solid electrolyte-solid electrolyte pairs. The horizontal dashed line demarks the compressive stress of 150 MPa required for complete dendrite deflection. The processing temperature values are upper bounds since they are calculated assuming fully dense solids and no plastic deformation under stress. Naturally, possible reactivity between components at fabrication temperature must be assessed in each case, but Figure C shows that the required residual stresses can be obtained with a very modest temperature change. It is seen that a modest quench can reach the threshold residual compressive stress of 150 MPa, only 50°C – 60°C for LATP and LLZO versus LFP, and \sim 60°C for LATP and LLZO versus LGPS. Thermal cycles of this magnitude are readily incorporated into electrolyte fabrication techniques producing dense electrolytes which reach maximum temperatures of 100°C-300°C.³⁸ On the other hand, for some materials combinations, a much larger temperature excursion is necessary and may be difficult to achieve. Figure 7D shows that the threshold stress is reached for a quench of 350°C for LiPON against LLZO, 39 550°C for LGPS against LFP, and 1,220°C for LATP against NMC. The results shown here are readily modified for alternative cell architectures and other materials, including composite electrolytes 40-43 (e.g., co-sintered cathodes/electrolytes; Figure 7B). The model

Please cite this article in press as: Fincher et al., Controlling dendrite propagation in solid-state batteries with engineered stress, Joule (2022), https://doi.org/10.1016/j.joule.2022.10.011





predicts that only three parameters, E', $\Delta \alpha$, and ΔT , are required to determine a critical compressive stress such as 150 MPa.

Deleterious effects of stack pressure on dendrite propagation

A stack pressure (σ_{xx} ; Figure 6A) has been widely used in previous studies and is observed to increase critical current densities and improve the uniformity of metal deposition. Stack pressures commonly vary from a few to several hundred MPa. 42,44–48 A previously unrecognized result, highlighted by Figure 6D, is that stack pressure is predicted by our model to have a deleterious effect by directing dendrite growth toward the electrode, promoting short-circuiting. 49 Figure 6D shows that, up to several times P, increasing stack pressures tend to decrease the propagation angle θ and ensure that dendrites will take a direct (rather than tortuous) path to penetrating the cell. The pressure applied to the cell in Figure 5 acts analogously to a stack pressure in a symmetric cell (σ_{xx} in Figure 6). Both the model in Figures 6D and 6E as well as the experiment in Figure 5 indicate that such pressures direct growing dendrites toward the stripping electrode, hastening short-circuit induced failure.

Conclusions

We propose a stress-based approach to mitigating metal-dendrite-induced failure in solid-state batteries. Using experiments and a fracture mechanics model, we show that metal dendrites growing through solid electrolytes can be deflected by an imposed stress. For Li-metal dendrites growing in LLZTO electrolyte, a compressive in-plane stress is observed to deflect the dendrite growth trajectory toward the compressive loading axis. The experiment and model also show that regardless of the initial orientation of a growing dendrite, a critical stress of $\sim\!150$ MPa applied in-plane can deflect growing dendrites sufficiently to avoid short circuits. This insight is used to propose materials combinations and processing approaches wherein residual stresses resulting from thermal expansion mismatch could be used to produce desirable stresses in laminate solid-state battery architectures.

These results help to resolve an existing controversy as to whether metal-dendrite propagation is dominated by fracture or by internal reduction of lithium ions to lithium metal. The experiments here are conducted under conditions where dendrite growth due to internal reduction of lithium ions remains possible, yet no evidence of such growth occurs when stress deflection is active. Thus, we conclude that, at least for the materials tested here, metal-dendrite propagation proceeds by mechanical fracture rather than electronic-conduction-based internal Li⁺ reduction.

EXPERIMENTAL PROCEDURES

Resource availability

Lead contact

Further information and requests should be directed to the corresponding author, Yet-Ming Chiang (ychiang@mit.edu).

Materials availability

This study did not generate new unique materials.

Data and code availability

All data and code are available from the authors upon request.





Cell preparation and assembly

Polycrystalline LLZTO was obtained from Toshima Manufacturing Inc. (Saitama, Japan) as 1-mm-thick, 12.7-mm-diameter pellets. The phase purity of these pellets was confirmed via X-ray diffraction; the bulk conductivity and grain size were measured as 1.03 mS/cm and near 3 μ m, respectively, in the previous work of Park et al. LLZTO electrolytes were then mechanically polished to the end thickness specified within the text, using oil-based 1- μ m diamond suspension for the last polishing step. Immediately after polish, the electrolyte disks were transferred into an oven within an Ar-containing glovebox. The disks were heat treated at 500°C for 3 h.

The Li-metal/LLZTO interface was formed using similar methods to previous works. ^{2,10} Specifically, after heat treatment, the electrolyte disks were removed from the oven. Li-metal foil (Alfa Aesar, Ward Hill, Massachusetts, USA) was scraped with a steel spatula to produce a clean metal surface. This Li was then cut into 3-mm-diameter pads using a biopsy punch. The Li-metal pads were immediately adhered to the LLZTO disk, and the resulting assembly was placed into the oven and baked at 250°C for 1 h.

The resulting plan-view cells were fixed to a cantilever bar using Loctite 401 adhesive. For the experiment shown in Figure 3A, a 1/8"-thick, 1"-wide, 2'-long 6061 aluminum bar (McMaster, Elmhurst, Illinois, United States) was used. All other experiments used 1/2"-thick, 1"-wide, 2'-long acrylic bars (McMaster, Elmhurst, Illinois, United States). A strain gauge was fixed to the cantilever in a manner identical to the cell. The adhesive was allowed to cure for 3 h. Following this, the bar was fixed to a rigid frame as shown in Figure 1. The cell and strain gauge were located approximately 18" from the free end of the cantilever. Tungsten probe tips were inserted into the Li-metal electrodes so as to provide an electrical connection to a VMP-3 potentiostat (Biologic, Knoxville, Tennessee, USA). This electrical connection permitted controlled electrochemical cycling within the glovebox.

Operando measurements

Operando optical measurements were recorded using a Leica DMS300 microscope, with the sample backlit using an LED plate. Electrochemical cycling and measurement were conducted using a VMP-3 potentiostat (Biologic, Knoxville, Tennessee, USA). All currents discussed in the text were applied to the cell galvanostatically, with the current density representing the applied current divided by the initial Li electrode area.

Meanwhile, strain measurements were collected from a strain gauge (CEA-06-250UN-350/P2, Micro-Measurements, Raleigh, North Carolina, USA) fixed adjacent to the cell. Strain data (ε_{gauge}) was collected in real time using a D4 Data acquisition system (Micro-Measurements, Raleigh, North Carolina, USA). The distance from the end of the bar for both the sample (L_{elyte}) and the strain gauge (L_{gauge}) are measured using a ruler. Because the gauge and the sample are positioned at different distances from the end of the bar, they possess slightly different strains. Thus, the strain in the electrolyte can be estimated by correcting the strain in the gauge using beam bending theory. From Euler-Bernoulli beam bending theory, ²⁵ the axial strain at a point on the surface of the cantilever can be written as

$$\varepsilon = \frac{6WL}{E_{cantilever}bh^3}$$

with W as the weight applied to the free end of the cantilever, L as the distance from the end of the cantilever, b as the length of the cantilever's base, and h as the height





of the cantilever. From the above equation, we know that (for a constant load) the value of ε/L is constant everywhere on the bar. In testing, holding a test cantilever and gauge loaded for a period of several hours did not yield a significant change in the measured strain. Therefore, we can conclude that the gauge and the sample are rigidly fixed to the cantilever. Thus, the average strain in the electrolyte ($\epsilon_{\rm elyte}$) is related to the measured strain in the gauge by

$$\frac{\varepsilon_{elyte}}{L_{elyte}} = \frac{\varepsilon_{gauge}}{L_{gauge}} {\rightarrow} \varepsilon_{elyte} = \varepsilon_{gauge} \bigg(\frac{L_{elyte}}{L_{gauge}} \bigg).$$

The electrolyte strain along the cantilever's axis was calculated from the measured strain based upon the above equation. Given that the radius r_{elyte} of the electrolyte (0.25'') is very small compared with the distance from the end of the bar (\sim 18"), the strain state differs minimally at the edges of the electrolyte as compared with the center of the electrolyte ($\varepsilon_{elyte\ edges} = \frac{L_{elyte}\pm r_{elyte}}{L_{elyte}} = (1\pm0.014)\varepsilon_{elyte}$). Because the electrolyte is very thin compared with the cantilever, the cantilever effectively prevents the electrolyte from straining perpendicular to the bar's axis. Thus, other strains within the plane of the bar's surface can be neglected, yielding a plane strain elastic problem. From Hooke's law, we can state the stress along the bar's axis ($\sigma_{applied}$) as:

$$\sigma_{applied} = \frac{E_{LLZTO}}{1 - v^2} \varepsilon_{elyte}$$

The measured stresses reported within the main text and supplemental information are then reported as $\sigma_{applied}$ while taking E_{LLZTO} and ν LLZTO as 150 GPa and 0.25, respectively.⁵⁰

In order to calibrate our apparatus, we first adhered a strain gauge (which has high compliance) to the cantilever in order to establish a baseline response. Then, we applied a second strain gauge to the surface of a 90-µm-thick LLZTO solid electrolyte adhered to the same cantilever. The response of the two strain gauges were within 15% of each other. Furthermore, the gauge reading from the gauge mounted on top of the LLZTO varied by less than 5% over 5 loading cycles. This shows that the adhesion of the solid electrolyte is secure through multiple loading cycles.

Analytical methods

Predicting kink angle from mixed-mode fracture mechanics

The configurations in Figures 1 and 7 can both be analyzed with standard 2D frameworks (plane stress and plane strain, respectively). In both cases, the maximum strain energy release rate for a crack at angle 90° $-\beta$ from the direction of a normal load occurs at the kink angle α which maximizes the local mode I stress intensity factor k, defined as⁵¹:

$$k_{I}(\alpha) = C_{11}K_{I} + C_{12}K_{II}$$
 (Equation 1)

where K_{l} and K_{ll} are the stress intensity factors for mode I and mode II such that

$$K_{l} = K_{l(0)} \cos^{2} \beta$$
 (Equation 2)

$$K_{l} = K_{l(0)}\cos^{2}\beta$$
 (Equation 2)
 $K_{ll} = K_{l(0)}\cos\beta\sin\beta$ (Equation 3)

where $K_{I(0)}$ represents the stress intensity factor if the crack was at $\beta = 0$. Taking the prefactor and crack length as unity yields:

$$K_{I(0)} = \sigma$$
 (Equation 4)

With σ as the applied load, and where C_{11} , C_{12} are coefficients such that

$$C_{11}(\alpha) = \frac{3}{4}\cos\left(\frac{\alpha}{2}\right) + \frac{1}{4}\cos\left(\frac{3\alpha}{2}\right)$$
 (Equation 5)





$$C_{12}(\alpha) = -\frac{3}{4} \left[\sin\left(\frac{\alpha}{2}\right) + \sin\left(\frac{3\alpha}{2}\right) \right]$$
 (Equation 6)

With α being the angle of the kink from the plane of the crack.

In the problem of interest, we have two applied stresses, which can be superimposed to predict the kink angle for a growing crack: (1) a plating-induced mode I load P of unit pressure and (2) an applied normal (compressive) load of $\widehat{\sigma} = \frac{\sigma_{applied}}{P}$ aligned with the bar's axis, acting upon a crack oriented at angle $90^{\circ} - \beta$. This second load represents the external compression on the electrolyte. The plating-induced pressure is applied normal to the crack faces, and oriented at an angle of β relative to the coordinate system of load 2. Thus, the remotely applied stress state can be described using superposition as:

$$R(\beta)\begin{bmatrix} 0 & 0 \\ 0 & 1 \end{bmatrix}R^{\mathsf{T}}(\beta) + \begin{bmatrix} -\nu\widehat{\sigma} & 0 \\ 0 & -\widehat{\sigma} \end{bmatrix} = \begin{bmatrix} \sigma_{xx} & \sigma_{xy} \\ \sigma_{xy} & \sigma_{yy} \end{bmatrix}$$
 (Equation 7)

where R is the rotation matrix:

$$R(\theta) = \begin{bmatrix} \cos\theta & -\sin\theta \\ \sin\theta & \cos\theta \end{bmatrix}$$
 (Equation 8)

This system can be rotated by an angle θ' to give the principal stress state, such that

$$R(\theta' + \beta) \begin{bmatrix} 0 & 0 \\ 0 & 1 \end{bmatrix} R^{\mathsf{T}}(\theta' + \beta) + R(\theta') \begin{bmatrix} -\nu \widehat{\sigma} & 0 \\ 0 & -\widehat{\sigma} \end{bmatrix} R(\theta') = \begin{bmatrix} \sigma_1 & 0 \\ 0 & \sigma_2 \end{bmatrix}$$
 (Equation 9)

where σ_1 and σ_2 are the principal stresses, with $\sigma_1 > \sigma_2$. The exact values of σ_1 , σ_2 , and θ' are determined by the eigenvalues and eigenvectors of the initial system for a given value of $\widehat{\sigma}$ and β . This allows for the determination of the local stress intensity factor by superimposing two principal stresses at 90° to one another, permitting Equations 2, 3, and 4 to be rewritten as

$$K_{I} = \left[\sigma_{1}\cos^{2}(\beta - \theta') + \sigma_{2}\sin^{2}(\beta - \theta')\right]$$
 (Equation 10)

$$K_{II} = \left[(\sigma_{1} - \sigma_{2})\sin(\beta')\cos(\beta - \theta')\right]$$
 (Equation 11)

The most energetically favorable kink angle, α^* , is then defined as the angle α that maximizes the local stress intensity factor, k_I , now rewritten from Equations 1, 10, and 11 as

$$k_{I}(\alpha) = C_{11}(\alpha) \left[\sigma_{1} \cos^{2}(\beta - \theta') + \sigma_{2} \sin^{2}(\beta - \theta') \right] + C_{12}(\alpha) \left[\times (\sigma_{1} - \sigma_{2}) \sin(\beta - \theta') \cos(\beta - \theta') \right]$$
 (Equation 12)

We determine this optimum angle α^* analytically. Because this kink angle is relative to the initial crack orientation, the direct sum of the most favorable kink angle α^* to the crack angle β yields the ultimate propagation angle $\theta = \alpha^* + \beta$ discussed in the text.

We note that this analysis considers only the most favorable angle of dendritic propagation, which is directly relevant to the amount of material that must be plated prior to failure. A smaller propagation angle implies that more metal plating must occur before dendrite-induced shorting, while a larger angle implies the opposite. However, this analysis does not directly consider the exact value of the driving force after the crack kinks, nor does it investigate the impact of the electric field on propagation. Furthermore, we have assumed the electrolyte to be isotropic and homogeneous. In reality, electrolytes possess microstructural features and defects, which may impact the mechanics and thus morphology of propagating flaws.

In the above analysis, the kink angle possesses no direct dependence on flaw size. For a channel crack in a thin film, the critical pressure for fracture possesses no





flaw length dependence, so long as the flaw is substantially longer than the film thickness. This greatly simplifies analysis of the plan-view cells outlined here. For a conventional cell format, an indirect dependence on flaw size occurs via the dependence of P on the flaw size. In applying this analysis to sandwich-style cells, we must assume a representative flaw size and stress intensity factor for failure to estimate a representative P. As discussed in the main text, we use $a=10~\mu m$ and $K_c=1~MPa \cdot \sqrt{m}$. We note that for flaws initially smaller than the representative 10 μm used here, the initial value of P is higher. However, with propagation, the value of P decreases until reaching that of the representative flaw discussed here. Thus, the analysis outlined herein should still apply.

Estimating the mechanical pressure to propagate a channel crack in a thin film

We estimate the mechanical pressure to propagate a channel crack in an LLZTO film on the cantilever substrate, as shown in Figure 3A. We treat the dendrite shown in Figure 3A as a channel crack propagating through a thin film bonded to a semi-infinite elastic substrate. Both the film and the substrate are treated as isotropic, homogeneous, linear elastic materials with known Young's modulus E and Poisson ratio ν . Treating this cracking as a plane strain problem, the material dependence depends on the two dimensionless parameters α_d and β_d (the Dundurs parameters), 18 such that

$$\begin{split} \alpha_{d} \; &= \; \frac{\overline{E}_{\mathit{film}} - \overline{E}_{\mathsf{sub.}}}{\overline{E}_{\mathit{film}} + \overline{E}_{\mathsf{sub}}} \beta_{d} \; &= \; \frac{\mu_{\mathit{film}} (1 - 2 \nu_{\mathsf{sub.}}) - \mu_{\mathsf{sub.}} (1 - 2 \nu_{\mathit{film}})}{2 \mu_{\mathit{film}} (1 - \nu_{\mathsf{sub.}}) + 2 \mu_{\mathsf{sub.}} (1 - \nu_{\mathit{film}})} \\ G_{\mathsf{ss.}} \; &= \; g(\alpha_{d}, \beta_{d}) \frac{\pi}{2} \frac{\sigma^{2} t_{\mathit{film}}}{\overline{E}_{\mathit{film}}} \end{split}$$

Where g is a function of the Dundurs parameters outlined by Beuth, and t_{film} is the film thickness. For crack propagation, this strain energy release rate must be equal to the critical strain energy release rate for fracture (Γ), which can be related to measured K_{1C} values as follows:

$$\Gamma = \frac{K_{1C}^2}{\overline{E}_{film}} = g(\alpha_d, \beta_d) \frac{\pi}{2} \frac{{\sigma_{crit.}}^2 t_{film}}{\overline{E}_{film}}$$

Thus, solving for the critical stress $\sigma_{crit.}$ yields

$$\sigma_{crit.} = \sqrt{\frac{1}{g(\alpha_d, \beta_d)} \frac{2}{\pi} \frac{K_{1C}^2}{t_{film}}}$$

In modeling the LLZTO film, we take $E_{film}=150$ GPa and $\nu=0.25$ as from Yu et al. ⁵⁰ Meanwhile, we consider the elastic properties of the cantilever (6061 aluminum for Figure 3A) as $E_{sub.}=70$ GPa and $\nu=0.25$. These material properties yield Dundurs parameters of $\alpha_d=0.36$ and $\beta_d=0.04$, where $g(\alpha_d=0.36,\ \beta_d=0.04)=1.74$. The LLZTO film shown in Figure 3A was measured as 90 μ m using an optical microscope (BA 310 met, Motic, Barcelona, Spain) with 50× objective. The actual K_{1C} (based upon indentation fracture toughness measurements ^{2,19}) appears to vary between 1—2 MPa \sqrt{m} , as would be expected for a brittle ceramic. Taking 1 and 2 MPa \sqrt{m} as upper and lower bounds produces $\sigma_{crit.}$ between 65 and 120 MPa \sqrt{m} .

Where \overline{E} is the plane strain modulus, $\overline{E}=E/(1-\nu^2)$, and μ is the shear modulus, $\mu=2E/(1+\nu)$. The only two length scales present in this problem are the film thickness and the crack length. According to Nakamura and Kamath, ³² in the limit that the crack length is larger than the film thickness, the strain energy release rate (and thus stress intensity factor) is independent of crack length. This allows us to invoke the analysis from Beuth ¹⁸ to estimate the steady state energy release rate ($G_{ss.}$) for a uniform stress σ on the crack face.





SUPPLEMENTAL INFORMATION

Supplemental information can be found online at https://doi.org/10.1016/j.joule. 2022.10.011.

ACKNOWLEDGMENTS

C.D.F. acknowledges the support of a National Science Foundation Graduate Research Fellowship under grant no. 1746932 and later by a Department of Defense National Science and Engineering Graduate Fellowship. Y.-M.C. acknowledges support from the US Department of Energy, Office of Basic Energy Science, through award no. DE-SC0002633 (J. Vetrano, Program Manager) during the early stages of the project, and later by the DARPA MINT program through contract no. HR00112220032 (V. Sundaresan, Program Manager). M.J.W. was supported by DARPA MINT, also through contract no. HR00112220032. C.E.A. and B.W.S. acknowledge support from the National Science Foundation (DMR-2124775).

AUTHOR CONTRIBUTIONS

C.D.F. and Y.-M.C. conceptualized the study. C.D.F. designed and executed the experiments and analyzed the data with input from all authors. C.D.F. developed the mixed-mode fracture model with input from C.G., W.C.C., and B.S. Y.-M.C. and C.D.F. developed the concepts for internally stressed batteries. C.D.F. wrote the first draft of the manuscript.

DECLARATION OF INTERESTS

Massachusetts Institute of Technology has filed for patents on subject matter related to this manuscript in which C.D.F., B.W.S., W.C.C., and Y.M.C. are listed inventors.

Received: July 19, 2022 Revised: September 26, 2022 Accepted: October 21, 2022 Published: November 18, 2022

REFERENCES

- Albertus, P., Babinec, S., Litzelman, S., and Newman, A. (2018). Status and challenges in enabling the lithium metal electrode for high-energy and low-cost rechargeable batteries. Nat. Energy 3, 16–21.
- 2. Park, R.J.-Y., Eschler, C.M., Fincher, C.D., Badel, A.F., Guan, P., Pharr, M., Sheldon, B.W., Carter, W.C., Viswanathan, V., and Chiang, Y.-M. (2021). Semi-solid alkali metal electrodes enabling high critical current densities in solid electrolyte batteries. Nat. Energy 6, 314–322.
- 3. Han, F., Westover, A.S., Yue, J., Fan, X., Wang, F., Chi, M., Leonard, D.N., Dudney, N.J., Wang, H., and Wang, C. (2019). High electronic conductivity as the origin of lithium dendrite formation within solid electrolytes. Nat. Energy 4, 187–196. https://doi.org/10.1038/s41560-018-0312-z.
- Armstrong, R.D., Dickinson, T., and Turner, J. (1974). The breakdown of β-alumina ceramic electrolyte. Electrochim. Acta 19, 187–192. https://doi.org/10.1016/0013-4886(74)85065-6.

- De Jonghe, L.C., Feldman, L., and Beuchele, A. (1981). Slow degradation and electron conduction in sodium/beta-aluminas. J. Mater. Sci. 16, 780–786.
- Liu, X., Garcia-Mendez, R., Lupini, A.R., Cheng, Y., Hood, Z.D., Han, F., Sharafi, A., Idrobo, J.C., Dudney, N.J., Wang, C., et al. (2021). Local electronic structure variation resulting in Li 'filament' formation within solid electrolytes. Nat. Mater. 20, 1485–1490. https://doi.org/10. 1038/s41563-021-01019-x.
- Zhao, J., Tang, Y., Dai, Q., Du, C., Zhang, Y., Xue, D., Chen, T., Chen, J., Wang, B., Yao, J., et al. (2022). In situ Observation of Li Deposition-Induced Cracking in Garnet Solid Electrolytes. Energy & Environ. Materials 5, 524–532. https://doi.org/10.1002/eem2.12261.
- 8. Porz, L., Swamy, T., Sheldon, B.W., Rettenwander, D., Frömling, T., Thaman, H.L., Berendts, S., Uecker, R., Carter, W.C., and Chiang, Y.-M. (2017). Mechanism of lithium metal penetration through inorganic solid electrolytes. Adv. Energy Mater. 7, 1701003.
- 9. Sharafi, A., Meyer, H.M., Nanda, J., Wolfenstine, J., and Sakamoto, J. (2016).

- Characterizing the Li–Li₇La₃Zr₂O₁₂ interface stability and kinetics as a function of temperature and current density. J. Power Sources 302, 135–139.
- Kazyak, E., Garcia-Mendez, R., LePage, W.S., Sharafi, A., Davis, A.L., Sanchez, A.J., Chen, K.-H., Haslam, C., Sakamoto, J., and Dasgupta, N.P. (2020). Li penetration in ceramic solid electrolytes: operando microscopy analysis of morphology, propagation, and reversibility. Matter 2, 1025–1048. https://doi.org/10.1016/j. matt.2020.02.008.
- Swamy, T., Park, R., Sheldon, B.W., Rettenwander, D., Porz, L., Berendts, S., Uecker, R., Carter, W.C., and Chiang, Y.-M. (2018). Lithium metal penetration induced by electrodeposition through solid electrolytes: example in single-crystal Li₆La₃ZrTaO₁₂ garnet. J. Electrochem. Soc. 165, A3648–A3655.
- Ning, Z., Jolly, D.S., Li, G., De Meyere, R., Pu, S.D., Chen, Y., Kasemchainan, J., Ihli, J., Gong, C., Liu, B., et al. (2021). Visualizing platinginduced cracking in lithium-anode solidelectrolyte cells. Nat. Mater. 20, 1121–1129. https://doi.org/10.1038/s41563-021-00967-8.





- Qi, Y., Ban, C., and Harris, S.J. (2020). A new general paradigm for understanding and preventing Li metal penetration through solid electrolytes. Joule 4, 2599–2608. https://doi. org/10.1016/j.joule.2020.10.009.
- Reisecker, V., Flatscher, F., Porz, L., Fincher, C., Hanghofer, I., Hennige, V., Linares-Moreau, M., Falcaro, P., Ganschow, S., and Wenner, S. (2022). The impact of pulsed current waveforms on Li dendrite initiation and propagation in solid-state Li batteries. ChemRxiv. https://doi. org/10.26434/chemrxiv-2022-6dpzs.
- McConohy, G., Xu, X., Cui, T., Barks, E., Wang, S., Kaeli, E., Melamed, C., Gu, X.W., and Chueh, W.C. (2022). Mechanical origins of lithium-metal intrusions into garnet solid electrolytes revealed by failure statistics. ChemRxiv. https://doi.org/10.26434/chemrxiv-2022-332(0).
- Williams, J.G., and Ewing, P.D. (1972). Fracture under complex stress—the angled crack problem. Int. J. Fract. Mech. 8, 441–446.
- Cotterell, B., and Rice, J.R., Jr. (1980). Slightly curved or kinked cracks. Int. J. Fract. 16, 155–169.
- Beuth, J.L., Jr. (1992). Cracking of thin bonded films in residual tension. Int. J. Solids Struct. 29, 1657–1675.
- Wolfenstine, J., Jo, H., Cho, Y.-H., David, I.N., Askeland, P., Case, E.D., Kim, H., Choe, H., and Sakamoto, J. (2013). A preliminary investigation of fracture toughness of Li₇La₃Zr₂O₁₂ and its comparison to other solid li-ionconductors. Mater. Lett. 96, 117–120.
- Jagad, H.D., Harris, S.J., Sheldon, B.W., and Qi, Y. (2022). Tradeoff between the ion exchangeinduced residual stress and ion transport in solid electrolytes. Chem. Mater. 34, 8694–8704. https://doi.org/10.1021/acs.chemmater. 2c01806.
- 21. Fincher, C.D., Ojeda, D., Zhang, Y., Pharr, G.M., and Pharr, M. (2020). Mechanical properties of metallic lithium: from nano to bulk scales. Acta Mater. 186, 215–222.
- LePage, W.S., Chen, Y., Kazyak, E., Chen, K.-H., Sanchez, A.J., Poli, A., Arruda, E.M., Thouless, M.D., and Dasgupta, N.P. (2019). Lithium mechanics: roles of strain rate and temperature and implications for lithium metal batteries.
 J. Electrochem. Soc. 166, A89–A97.
- Masias, A., Felten, N., Garcia-Mendez, R., Wolfenstine, J., and Sakamoto, J. (2019). Elastic, plastic, and creep mechanical properties of lithium metal. J. Mater. Sci. 54, 2585–2600.
- Kim, S., Wee, J., Peters, K., and Huang, H.-Y.S. (2018). Multiphysics coupling in lithium-ion batteries with reconstructed porous microstructures. J. Phys. Chem. C 122, 5280–5290.
- 25. Gere, J.M., and Timoshenko, S.P. (1997). Mechanics of Materials (PWS).
- Hubaud, A.A., Schroeder, D.J., Ingram, B.J., Okasinski, J.S., and Vaughey, J.T. (2015). Thermal expansion in the garnet-type solid electrolyte (Li_{7-x}Al_{x/3}) La₃Zr₂O₁₂ as a function of Al content. J. Alloys Compd. 644, 804–807.

- Weber, D.A., Senyshyn, A., Weldert, K.S., Wenzel, S., Zhang, W., Kaiser, R., Berendts, S., Janek, J., and Zeier, W.G. (2016). Structural insights and 3D diffusion pathways within the lithium superionic conductor Li₁₀GeP₂S₁₂. Chem. Mater. 28, 5905–5915. https://doi.org/ 10.1021/acs.chemmater.6b02424.
- Athanasiou, C.E., Jin, M.Y., Ramirez, C., Padture, N.P., and Sheldon, B.W. (2020). Hightoughness inorganic solid electrolytes via the use of reduced graphene oxide. Matter 3, 212–229
- Athanasiou, C.E., Liu, X., Jin, M.Y., Nimon, E., Visco, S., Lee, C., Park, M., Yun, J., Padture, N.P., Gao, H., and Sheldon, B.W. (2022). Ratedependent deformation of amorphous sulfide glass electrolytes for solid-state batteries. Cell Rep. Phys. Sci. 3, 100845. https://doi.org/10. 1016/j.xcrp.2022.100845.
- Deng, Z., Wang, Z., Chu, I.-H., Luo, J., and Ong, S.P. (2016). Elastic properties of alkali superionic conductor electrolytes from first principles calculations. J. Electrochem. Soc. 163, A67–A74. https://doi.org/10.1149/2. 0061602jes.
- Yan, G., Yu, S., Nonemacher, J.F., Tempel, H., Kungl, H., Malzbender, J., Eichel, R.-A., and Krüger, M. (2019). Influence of sintering temperature on conductivity and mechanical behavior of the solid electrolyte LATP. Ceram. Int. 45, 14697–14703.
- 32. Nakamura, T., and Kamath, S.M. (1992). Threedimensional effects in thin film fracture mechanics. Mech. Mater. 13, 67–77.
- Herbert, E.G., Tenhaeff, W.E., Dudney, N.J., and Pharr, G.M. (2011). Mechanical characterization of LiPON films using nanoindentation. Thin Solid Films 520, 413-418.
- Cheng, E.J., Hong, K., Taylor, N.J., Choe, H., Wolfenstine, J., and Sakamoto, J. (2017). Mechanical and physical properties of LiNi_{0.33}Mn_{0.33}Co_{0.33}O₂ (NMC). J. Eur. Ceramic Soc. 37, 3213–3217.
- Lee, E., Muhammad, S., Kim, T., Kim, H., Lee, W., and Yoon, W.S. (2020). Tracking the influence of thermal expansion and oxygen vacancies on the thermal stability of Ni-rich layered cathode materials. Adv. Sci. (Weinh) 7, 1902413. https://doi.org/10.1002/advs. 201902413.
- Abadias, G., Chason, E., Keckes, J., Sebastiani, M., Thompson, G.B., Barthel, E., Doll, G.L., Murray, C.E., Stoessel, C.H., and Martinu, L. (2018). Stress in thin films and coatings: current status, challenges, and prospects. J. Vac. Sci. Technol. A 36, 020801.
- Jackman, S.D., and Cutler, R.A. (2012). Effect of microcracking on ionic conductivity in LATP. J. Power Sources 218, 65–72.
- Kim, K.J., Balaish, M., Wadaguchi, M., Kong, L., and Rupp, J.L.M. (2021). Solid-state Li-metal batteries: challenges and horizons of oxide and sulfide solid electrolytes and their interfaces. Adv. Energy Mater. 11, 2002689.
- Vereda, F., Clay, N., Gerouki, A., Goldner, R.B., Haas, T., and Zerigian, P. (2000). A study of electronic shorting in IBDA-deposited Lipon films. J. Power Sources 89, 201–205.

- https://doi.org/10.1016/S0378-7753(00) 00430-4.
- Hitz, G.T., McOwen, D.W., Zhang, L., Ma, Z., Fu, Z., Wen, Y., Gong, Y., Dai, J., Hamann, T.R., Hu, L., et al. (2019). High-rate lithium cycling in a scalable trilayer Li-garnet-electrolyte architecture. Mater. Today 22, 50–57. https:// doi.org/10.1016/j.mattod.2018.04.004.
- Fu, K. (Kelvin), Gong, Y., Hitz, G.T., McOwen, D.W., Li, Y., Xu, S., Wen, Y., Zhang, L., Wang, C., Pastel, G., et al. (2017). Three-dimensional bilayer garnet solid electrolyte based high energy density lithium metal–sulfur batteries. Energy Environ. Sci. 10, 1568–1575. https://doi. org/10.1039/C7EE01004D.
- Ye, L., and Li, X. (2021). A dynamic stability design strategy for lithium metal solid state batteries. Nature 593, 218–222. https://doi. org/10.1038/s41586-021-03486-3.
- Sastre, J., Futscher, M.H., Pompizi, L., Aribia, A., Priebe, A., Overbeck, J., Stiefel, M., Tiwari, A.N., and Romanyuk, Y.E. (2021). Blocking lithium dendrite growth in solid-state batteries with an ultrathin amorphous Li-La-Zr-O solid electrolyte. Commun. Mater. 2, 1–10.
- 44. Krauskopf, T., Hartmann, H., Zeier, W.G., and Janek, J. (2019). Toward a fundamental understanding of the lithium metal anode in solid-state batteries—an electrochemomechanical study on the garnet-type solid electrolyte Li_{6.25}Al_{0.25}La₃Zr₂O₁₂. ACS Appl. Mater. Interfaces 11, 14463–14477.
- 45. Krauskopf, T., Mogwitz, B., Rosenbach, C., Zeier, W.G., and Janek, J. (2019). Diffusion limitation of lithium metal and Li–Mg alloy anodes on LLZO type solid electrolytes as a function of temperature and pressure. Adv. Energy Mater. 9, 1902568.
- Doux, J.-M., Nguyen, H., Tan, D.H.S., Banerjee, A., Wang, X., Wu, E.A., Jo, C., Yang, H., and Meng, Y.S. (2020). Stack pressure considerations for room-temperature all-solid-state lithium metal batteries. Adv. Energy Mater. 10, 1903253.
- Meyer, A., Xiao, X., Chen, M., Seo, A., and Cheng, Y.-T. (2021). A power-law decrease in interfacial resistance between Li₇La₃Zr₂O₁₂ and lithium metal after removing stack pressure. J. Electrochem. Soc. 168, 100522.
- 48. Doux, J.-M., Yang, Y., Tan, D.H.S., Nguyen, H., Wu, E.A., Wang, X., Banerjee, A., and Meng, Y.S. (2020). Pressure effects on sulfide electrolytes for all solid-state batteries.
 J. Mater. Chem. A 8, 5049–5055.
- Poisson constraints may result in a decreased stress intensity factor for a laterally constrained stack, but this effect is not sufficient to prevent dendrite growth under any reasonable electrical potential.
- Yu, S., Schmidt, R.D., Garcia-Mendez, R., Herbert, E., Dudney, N.J., Wolfenstine, J.B., Sakamoto, J., and Siegel, D.J. (2016). Elastic properties of the solid electrolyte Li₇La₃Zr₂O₁₂ (LLZO). Chem. Mater. 28, 197–206.
- 51. Anderson, T.L. (2017). Fracture Mechanics: Fundamentals and Applications (CRC Press).